

Chemical models of adenine precursors cyanamide and carbodiimide in the interstellar medium

Xia Zhang,^{1,2} Donghui Quan,^{3,1*} Runxia Li,² Jarken Esimbek,^{1,2,4} Long-Fei Chen,³ Guoming Zhao⁵ and Yan Zhou⁶

¹ Xinjiang Astronomical Observatory, Chinese Academy of Sciences, 150 Science 1-Street, Urumqi, Xinjiang 830011, China

² Xinjiang Key Laboratory of Radio Astrophysics, 150 Science 1-Street, Urumqi 830011, China

³ Research Center for Intelligent Computing Platforms, Zhejiang Laboratory, Hangzhou 311100, China

⁴ Key Laboratory of Radio Astronomy, Chinese Academy of Sciences, Urumqi 830011, China

⁵ School of Science, Jilin Institute of Chemical Technology, Jilin, Jilin 132022, China

⁶ Binzhou University, Huanghe Road, Binzhou City, Shandong, 256600, China

Accepted XXX. Received YYY; in original form ZZZ

ABSTRACT

Cyanamide (NH₂CN) and its isomer, carbodiimide (HNCNH), may form adenine in the interstellar medium (ISM) via a series of reactions. Therefore, they are considered key prebiotic molecules in the study of the origin of life. We used the three-phase NAUTILUS chemical code, which includes the gas, the dust surface, and the icy mantle, to investigate the formation and destruction of cyanamide and carbodiimide. We added over 200 new chemical reactions of the two isomers and related species, and established a relatively complete network. We applied cold core, hot corino/core and shock models to simulate the different physical environments, and found that the two isomers are mainly produced by the free radical reactions on grain surfaces. Our simulated results suggest that cyanamide and carbodiimide molecules come from surface chemistry at early evolutionary stages. Then they are released back to the gas phase, either by thermal process (in hot cores, hot corinos) or shock-induced desorption (in shock regions). We speculate that it is an inefficient route to form a tautomer of adenine by starting from molecules cyanoacetylene (C₃NH), cyanamide and carbodiimide in ISM.

Key words: astrochemistry – molecular processes – ISM: abundances – ISM: molecules.

1 INTRODUCTION

How life on Earth began remains an unexplained scientific problem. Prebiotic chemistry addresses this issue through the aspects of theory, experiment and observation. However, large molecules of life such as ribonucleic acid RNA break down easily and are difficult to survive in the harsh interstellar environment. Therefore, they may be studied indirectly by their precursors: relatively small prebiotic molecules. Molecules containing cyano (CN) functional group are regarded as intermediates for the formation of purines and proteins (De Becker 2013). Adenine is one of purine of DNA and RNA nucleobases and is always presumed to be the product of HCN pentamer reaction (Chakrabarti & Chakrabarti 2000). However, Smith et al. (2001) found the reaction from HCN to adenine to be inefficient under interstellar medium (ISM) conditions. Merz et al. (2014) provided a new route for adenine synthesis, using the concept of retrosynthetic analysis to create a tautomer of adenine, starting from molecules cyanoacetylene (C₃NH), carbodiimide (HNCNH) and its isomer cyanamide (NH₂CN). Chakrabarti et al. (2015) proposed

that observers may look in the ISM for the two precursors C₃NH and HNCNH which are equally important for predicting abundances of adenine. Both C₃NH and HNCNH have been observed in the ISM (Kawaguchi et al. 1992; McGuire et al. 2012).

NH₂CN is one of the simplest organic molecules featuring cyano and amide groups. It is also the most stable of the isomers with the formula CH₂N₂. HNCNH is the second one, which is less stable than NH₂CN by about 4 kcal mol⁻¹ and therefore it is expected to be present in a smaller amount at thermal equilibrium (Jabs et al. 1999). The structural images of two isomers are shown in Fig. 1. NH₂CN is recognized as an important prebiotic molecule in the study of the origin of life (Steinman et al. 1964; Brack 1999). It can be converted into urea in liquid water (Kilpatrick 1947), while HNCNH can lead to isourea, a urea tautomer (Tordini et al. 2003). Urea has been observed to be present in Sgr B2(N1) (Belloche et al. 2019). However, Duvernay et al. (2004, 2005) did not detect the hydrolysis reaction of cyanamide or carbodiimide to form urea or isourea at low temperature (≤180 K) in their experimental study. Molecules with HNCNH moiety (-NCN-) are considered important condensing agents that are able to assemble amino acids into peptides in liquid water (Williams & Ibrahim 1981).

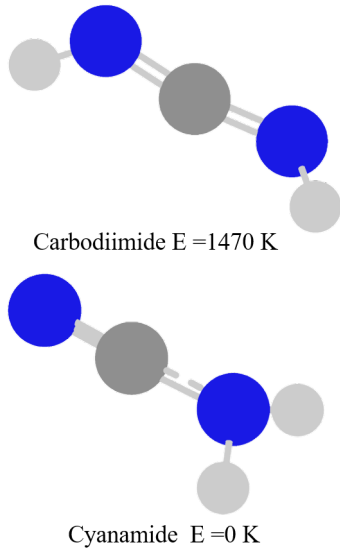
In the interstellar medium, NH₂CN was detected for the first

* E-mail: donghui.quan@zhejianglab.com

Table 1. Derived physical parameters of NH₂CN toward different types of sources.

Source name	T _{ex} (K)	N (cm ⁻²)	N (H ₂) (cm ⁻²)	Abundance	Reference
Sgr B2	20~60	0.2 ~ 6 × 10 ¹⁴	–	–	Turner et al. (1975)
Sgr B2(OH)	15	2 × 10 ¹³	5 × 10 ²³	4 × 10 ⁻¹¹	Cummins et al. (1986)
Sgr B2(N)	500	~ 2.3 × 10 ¹⁴	3 × 10 ²⁴	7.6 × 10 ⁻¹¹	Nummelin et al. (2000)
Sgr B2(N)	150	5.13(2.05) × 10 ¹⁶	–	–	Belloche et al. (2013)
Sgr B2(M)	68	3 × 10 ¹³	2 × 10 ²⁴	1.5 × 10 ⁻¹¹	Nummelin et al. (2000)
Orion-KL	100, 200	1.1, 0.33 × 10 ¹⁶	–	–	White et al. (2003)
NGC 253	67	1.2 × 10 ¹³	6.5 × 10 ²²	2 × 10 ⁻¹⁰	Martín et al. (2006)
M 82?	80.3	1.2 × 10 ¹³	–	–	Aladro et al. (2011)
G0.253+0.016	–	–	1.0 × 10 ²²	–	Rathborne et al. (2015)
IRAS 20126+4104	210	3.3 × 10 ¹⁵	2.7 × 10 ²⁴	1.2 × 10 ⁻⁹	Palau et al. (2017)
IRAS 16293-2422 B	100, 300	≥ 5, ≥ 7 × 10 ¹³	1.2 × 10 ²⁵	≤ 2 × 10 ⁻¹⁰	Coutens et al. (2018)
NGC 1333 IRAS2A	130	2.5 × 10 ¹⁴	5 × 10 ²⁴	~ 5 × 10 ⁻¹¹	Coutens et al. (2018)
NGC 1333 IRAS2A1	150	8.5 × 10 ¹⁴	5 × 10 ²⁴	~ 1.7 × 10 ⁻¹⁰	Belloche et al. (2020)
NGC 1333 IRAS4A2	150	8.5 × 10 ¹⁴	5 × 10 ²⁴	~ 1.7 × 10 ⁻¹⁰	Belloche et al. (2020)
SVS13A	220	2.5 × 10 ¹⁵	–	–	Belloche et al. (2020)
Barnard 1b?	60, 200	1.0, 1.0 × 10 ¹²	1.4, 1.1 × 10 ²⁵	7.1, 9.1 × 10 ⁻¹⁴	Marcelino et al. (2018)
G+0.693	6.3(ortho), 6.8(para)	3.8, 27 × 10 ¹³	1.35 × 10 ²³	2.3 × 10 ⁻⁹	Zeng et al. (2018)
NGC 6334I	135-285	2.3 – 78 × 10 ¹⁵	–	–	Ligterink et al. (2020)

Notes. ? tentative detection.

**Figure 1.** Optimized structures of the two isomers. Energies have been calculated at the CCSD(T)/aug-cc-pvtz//B2PLYPD3/may-cc-pvtz level. Blue, gray, white spheres correspond to nitrogen, carbon, and hydrogen atoms, respectively.

time toward Sgr B2 by Turner et al. (1975), with a column density of $2 \times 10^{14} \text{ cm}^{-2}$. Since then, it has been detected in several high-mass star forming regions, Sgr B2(N), Sgr B(M), Orion KL and NGC 6334I (Nummelin et al. 2000; White et al. 2003; Ligterink et al. 2020), the extragalactic sources, NGC 253 and M86 (Martín et al. 2006; Aladro et al. 2011), the molecular cluster G0.253+0.016 (Rathborne et al. 2015), the massive protostar IRAS 20126+4104 (Palau et al. 2017), two solar-type protostars, IRAS 16293-2422B and NGC 1333 IRAS2A (Coutens et al. 2018), the young protostar system Barnard 1B (Marcelino et al. 2018), and the quiescent giant molecular cloud, G+0.693-0.027 (hereafter G+0.693) (Zeng et al.

2018). A list of cyanamide with selected observed information is shown in Table 1.

In contrast to NH₂CN, HNCNH was only detected through weak maser emission toward the massive star formation region Sgr B2(N) using data from Green Bank Telescope (GBT) PRIMOS survey by McGuire et al. (2012). The column density of HNCNH was derived to be $2 \times 10^{13} \text{ cm}^{-2}$, which is about one order of magnitude lower than that of NH₂CN. Coutens et al. (2018) searched for HNCNH toward 16293-2422B and NGC1333 IRAS2A using ALMA Protostellar Interferometric Line Survey (PILS) and IRAM Plateau de Bure Interferometer (PdBI). However, HNCNH was not found and only a column density upper limit of $3 \times 10^{15} \text{ cm}^{-2}$ was set. Rivilla et al. (2021) also searched for HNCNH in the G+0.693 cloud and set an upper limit of $2.5 \times 10^{13} \text{ cm}^{-2}$.

In this work, we have added more than 200 reactions relating to NH₂CN and HNCNH to the KIDA 2016 network. We consider the experimentally approved or theoretically suggested reactions concerning these two isomers in the models. We proposed new reaction routes which were confirmed by quantum chemistry calculations, and present them in Section 2. We built astrochemical models to simulate the formation and destruction mechanisms of the two prebiotic molecules under the different physical conditions. Also, we explored the possible interstellar environment to form these molecules and illustrate them in Section 3. We discussed the implications of the results in Section 4, and draw conclusions in Section 5.

2 CHEMISTRY OF CYANAMIDE AND CARBODIIMIDE

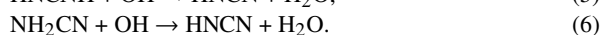
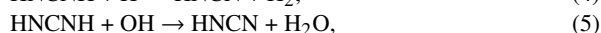
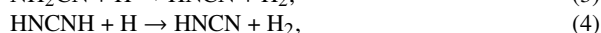
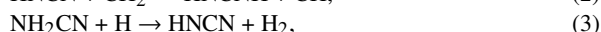
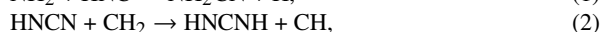
2.1 Formation and destruction of cyanamide and carbodiimide

The formation routes of cyanamide have been explored in many methods. Smith et al. (2004) proposed the reaction of CN + NH₃ → NH₂CN + H, but a high barrier was found to form NH₂CN and H in gas phase according to a theoretical study (Talbi & Smith 2009). Later, Blitz et al. (2009) experimentally confirmed that this

reaction was only the path to produce HCN and NH₂. [Sleiman et al. \(2018a\)](#) proposed the reaction between CN and CH₃NH₂ as an efficient route to form NH₂CN in ISM through low temperature kinetics experimental and theoretical studies. In their subsequent work, [Sleiman et al. \(2018b\)](#) further concluded that the route to form CH₂NH₂ + HCN is barrierless thus is the major production channel. [Puzzarini et al. \(2020\)](#) found CN + CH₃NH₂ has four reaction channels. [Coutens et al. \(2018\)](#) proposed the reaction of NH₂ and CN may directly form NH₂CN on grain surface.

Carbodiimide may be formed from the isomerization of cyanamide. The activation energy of this process is extremely high in gas phase, while it can be drastically reduced in the presence of water molecules ([Tordini et al. 2003](#)). [Duvernay et al. \(2004\)](#) confirmed that isomerization can become significant with water-ice at low temperatures by experiment. [Duvernay et al. \(2005\)](#) further verified through experiments that the isomerization reaction could occur by a photochemical process or when cyanamide is condensed at low temperature (50-140 K) on an amorphous water ice surface or trapped in the water ice, which acts like a catalyst. In addition, [He et al. \(1991\)](#) proposed three gas-phase reactions associated with HNCNH at high temperatures. [Yadav et al. \(2019\)](#) obtained two formation routes of HNCNH by quantum chemical calculation in gas phase or on grain surfaces. The first path is the reaction HNC + NH → HNCNH. The second one contains two steps: NH + CN → HNCN, followed by HNCN + H → HNCNH. However, in ISM, the addition reaction would hardly take place in such low-density gas due to the difficulty to release excess energy. Therefore, these addition reactions just occur on dust grains in ISM.

The chemistry of cyanamide and carbodiimide has been investigated by multiple research groups. But so far, no efficient gas-phase formation reactions have been proposed. The origin of cyanamide and carbodiimide in the ISM remains unclear. In this work, we ran quantum chemical calculations to evaluate the reactions of the two isomers and their related species. We found that the reaction of NH₂ + HNC and HNCN + CH₂ to produce NH₂CN and HNCNH, respectively, have relative high barriers (Reactions (1)-(2)). Besides, we list some key destruction reactions below (Reactions (3)-(6)).



In addition to the reactions mentioned above, two radicals can likely add together on the grain surface and are assumed to be barrierless (Reaction (7)-(9)), although when the radicals attach to water ice, there might be a barrier ([Enrique-Romero et al. 2019](#)). HNCN can form both cyanamide and carbodiimide through hydrogenation. Therefore, the formation we also propose reactions of HNCN (Reactions (8)-(9)).



Rate coefficients for gas-phase reactions of NH₂CN, HNCNH and related species are summarized in Table 2. The formulae that are used to calculate rate coefficients are categorized by different reaction types. For cosmic-ray induced photodissociation and UV

photodissociation, the formulae are expressed as follows: $k(T) = \alpha\zeta$, $k(T) = \alpha \exp(-\gamma A_v)$ respectively, where ζ is cosmic-ray ionization rate; A_v is the visual extinction (mag). The rate parameters of the cosmic-ray photodissociation and UV photodissociation reactions of cyanamide, carbodiimide and related species (HNCN, NCN) were estimated based on similar reactions already existing in the chemical network. Branching ratios to different product channels are often unmeasured for ion-molecule reactions that can lead to multiple products. To address this, we make the simplifying assumption that the different reaction channels occur equally, and thus have the same branching ratio. And the corresponding rate is calculated as $k(T) = \alpha\beta (0.62 + 0.4767 \gamma(300/T))$, except the reactions from [Woon & Herbst \(2009\)](#), where the corresponding rates are $k(T) = \alpha(T/300)^\beta \exp(-\gamma/T)$. This formula is also adopted for the neutral-neutral reactions and dissociative recombination reactions.

Related surface reactions are listed in Table 3 with their activation energy barriers. The barriers of free radical groups are assumed to be zero in this work. There is a high isomerization barrier between NH₂CN and HNCNH in the gas phase. But on ice surface, this barrier is low enough so that the reaction can take place even at a low temperature ([Duvernay et al. 2005](#)). Therefore, the surface isomerization reaction is added in the chemical reaction network in Table 3. As for the binding energies of NH₂CN and HNCNH, we adopt the value of 5556 K for both isomers, as listed in Table 4. Besides, the binding energies of all other newly added species are also included in the table.

2.2 Quantum chemical calculations

All quantum chemical calculations reported here were performed with the double-hybrid B2PLYP functions ([Grimme 2006](#)) combined with the may-cc-pVTZ basis set to optimize the structure and to calculate the frequency for all species and transition states involved in the study ([Dunning 1989](#); [Papajak et al. 2009](#)). Semi-empirical dispersion contributions were also included by means of the D3BJ model ([Goerigk & Grimme 2011](#); [Grimme et al. 2011](#)). Saddle points were assigned to reaction paths by using intrinsic reaction coordinate (IRC) ([Fukui 1981](#)) calculations at the same B2PLYP level as the identification of reactants and products. To achieve accurate energies for the stationary points from the optimization at the B2PLYPD3/may-cc-pVTZ level, the highly cost-effective method of CCSD(T) ([Purvis III & Bartlett 1982](#); [Scuseria et al. 1988](#); [Scuseria & Schaefer III 1989](#)), together with the basis sets aug-cc-pVTZ was further used. All quantum chemical calculations were run with the GAUSSIAN 16 program ([Frisch et al. 2016](#)).

Table 2: Summary of the rate coefficients of gas-phase reactions involving cyanamide, carbodiimide and related species.

Reaction	α	β	γ	Ref.
Cosmic Ray Induced Photodissociation				
	(-)	(-)	(-)	
NH ₂ CN → NH ₂ + CN	9.50E+03	0	0	Harada et al. (2010)
NH ₂ CN → H + HNCN	9.50E+03	0	0	This work
HNCNH → NH + HNC	9.50E+03	0	0	This work
HNCNH → H + HNCN	9.50E+03	0	0	This work
HNCN → N ₂ + CH	9.50E+03	0	0	Bise et al. (2001)
HNCN → HCN + N	9.50E+03	0	0	Bise et al. (2001)
HNCN → HNC + N	9.50E+03	0	0	Bise et al. (2001)
HNCN → NCN + H	9.50E+03	0	0	Bise et al. (2001)
NCN → N ₂ + C	9.50E+03	0	0	Bise et al. (1999)
NCN → N + CN	9.50E+03	0	0	Bise et al. (1999)
Photodissociation				
	(s ⁻¹)	(-)	(-)	
NH ₂ CN → NH ₂ + CN	1.00E-09	0	1.7	OSU database
NH ₂ CN → H + HNCN	1.00E-09	0	1.7	This work
HNCNH → NH + HNC	1.00E-09	0	1.7	This work
HNCNH → H + HNCN	1.00E-09	0	1.7	This work
HNCN → N ₂ + CH	1.00E-09	0	1.7	Bise et al. (2001)
HNCN → HCN + N	1.00E-09	0	1.7	Bise et al. (2001)
HNCN → HNC + N	1.00E-09	0	1.7	Bise et al. (2001)
HNCN → NCN + H	1.00E-09	0	1.7	Bise et al. (2001)
NCN → N ₂ + C	1.00E-09	0	1.7	Bise et al. (1999)
NCN → N + CN	1.00E-09	0	1.7	Bise et al. (1999)
Ion-neutral				
	(-)	(cm ³ s ⁻¹)	(-)	
C ⁺ + NH ₂ CN → NH ₂ CN ⁺ + C	0.50	1.48E-09	8.57	This work
C ⁺ + NH ₂ CN → C ₂ N ⁺ + NH ₂	0.50	1.48E-09	8.57	This work
C ⁺ + HNCNH → HNCNH ⁺ + C	0.50	1.57E-09	3.66	This work
C ⁺ + HNCNH → HNCN + CH ⁺	0.50	1.57E-09	3.66	This work
H ⁺ + NH ₂ CN → NH ₂ + HNC ⁺	0.50	4.73E-09	8.13	Woon & Herbst (2009)
H ⁺ + NH ₂ CN → NH ₂ ⁺ + HNC	0.50	4.73E-09	8.13	Woon & Herbst (2009)
H ⁺ + HNCNH → HNC ⁺ + NH ₂	0.50	4.85E-09	3.66	This work
H ⁺ + HNCNH → HNC + NH ₂ ⁺	0.50	4.85E-09	3.66	This work
He ⁺ + NH ₂ CN → NH ₂ + CN ⁺ + He	0.50	2.45E-09	8.13	Woon & Herbst (2009)
He ⁺ + NH ₂ CN → NH ₂ ⁺ + CN + He	0.50	2.45E-09	8.13	Woon & Herbst (2009)
He ⁺ + HNCNH → HNC ⁺ + NH + He	0.50	2.51E-09	3.66	This work
He ⁺ + HNCNH → HNC + NH ⁺ + He	0.50	2.51E-09	3.66	This work
H ₃ ⁺ + NH ₂ CN → NH ₂ CNH ⁺ + H ₂	0.50	2.79E-09	8.13	Woon & Herbst (2009)
H ₃ ⁺ + NH ₂ CN → HCN ⁺ + NH ₂ + H ₂	0.50	2.79E-09	8.13	This work
H ₃ ⁺ + HNCNH → NH ₂ CNH ⁺ + H ₂	0.33	2.86E-09	3.66	This work
H ₃ ⁺ + HNCNH → HNC ⁺ + NH ₂ + H ₂	0.33	2.86E-09	3.66	This work
H ₃ ⁺ + HNCNH → HNC + NH ₂ ⁺ + H ₂	0.33	2.86E-09	3.66	This work
H ₃ O ⁺ + NH ₂ CN → HCN ⁺ + NH ₂ + H ₂ O	0.50	1.25E-09	8.57	This work
H ₃ O ⁺ + NH ₂ CN → NH ₂ CNH ⁺ + H ₂ O	0.50	1.25E-09	8.57	This work
H ₃ O ⁺ + HNCNH → NH ₂ CNH ⁺ + H ₂ O	0.33	1.33E-09	3.66	This work
H ₃ O ⁺ + HNCNH → HNC ⁺ + NH ₂ + H ₂ O	0.33	1.33E-09	3.66	This work
H ₃ O ⁺ + HNCNH → HNC + NH ₂ ⁺ + H ₂ O	0.33	1.33E-09	3.66	This work
HCO ⁺ + NH ₂ CN → NH ₂ CNH ⁺ + CO	0.50	1.13E-09	8.13	Woon & Herbst (2009)
HCO ⁺ + NH ₂ CN → HCN ⁺ + NH ₂ + CO	0.50	1.13E-09	8.13	This work
HCO ⁺ + HNCNH → NH ₂ CNH ⁺ + CO	0.33	1.16E-09	3.66	This work
HCO ⁺ + HNCNH → HNC ⁺ + NH ₂ + CO	0.33	1.16E-09	3.66	This work
HCO ⁺ + HNCNH → HNC + NH ₂ ⁺ + CO	0.33	1.16E-09	3.66	This work
He ⁺ + HNCN → CN ⁺ + NH + He	0.50	2.39E-09	5.30	This work
He ⁺ + HNCN → CN + NH ⁺ + He	0.50	2.39E-09	5.30	This work
C ⁺ + HNCN → HNCN ⁺ + C	0.50	1.50E-09	5.30	This work
C ⁺ + HNCN → NCN + CH ⁺	0.50	1.50E-09	5.30	This work
H ⁺ + HNCN → NCN ⁺ + H ₂	0.50	4.61E-09	5.30	This work
H ⁺ + HNCN → HNCN ⁺ + H	0.50	4.61E-09	5.30	This work
H ₃ ⁺ + HNCN → HNCNH ⁺ + H ₂	0.33	2.73E-09	5.30	This work
H ₃ ⁺ + HNCN → HNC ⁺ + NH + H ₂	0.33	2.73E-09	5.30	This work

Continuation of Table 2

Reaction	α	β	γ	Ref.
$\text{H}_3^+ + \text{HNCN} \rightarrow \text{HNC} + \text{NH}^+ + \text{H}_2$	0.33	2.73E-09	5.30	This work
$\text{H}_3\text{O}^+ + \text{HNCN} \rightarrow \text{HNCNH}^+ + \text{H}_2\text{O}$	0.33	1.26E-09	5.30	This work
$\text{H}_3\text{O}^+ + \text{HNCN} \rightarrow \text{HNC}^+ + \text{NH} + \text{H}_2\text{O}$	0.33	1.26E-09	5.30	This work
$\text{H}_3\text{O}^+ + \text{HNCN} \rightarrow \text{HNC} + \text{NH}^+ + \text{H}_2\text{O}$	0.33	1.26E-09	5.30	This work
$\text{HCO}^+ + \text{HNCN} \rightarrow \text{HNCNH}^+ + \text{CO}$	0.33	1.11E-09	5.30	This work
$\text{HCO}^+ + \text{HNCN} \rightarrow \text{HNC}^+ + \text{NH} + \text{CO}$	0.33	1.11E-09	5.30	This work
$\text{HCO}^+ + \text{HNCN} \rightarrow \text{HNC} + \text{NH}^+ + \text{CO}$	0.33	1.11E-09	5.30	This work
$\text{He}^+ + \text{NCN} \rightarrow \text{CN}^+ + \text{N} + \text{He}$	0.50	2.27E-09	1.69	This work
$\text{He}^+ + \text{NCN} \rightarrow \text{CN} + \text{N}^+ + \text{He}$	0.50	2.27E-09	1.69	This work
$\text{C}^+ + \text{NCN} \rightarrow \text{NCN}^+ + \text{C}$	0.50	1.43E-09	1.69	This work
$\text{C}^+ + \text{NCN} \rightarrow \text{CN} + \text{CN}^+$	0.50	1.43E-09	1.69	This work
$\text{H}^+ + \text{NCN} \rightarrow \text{NCN}^+ + \text{H}$	0.50	4.39E-09	1.69	This work
$\text{H}^+ + \text{NCN} \rightarrow \text{CN}^+ + \text{NH}^+$	0.50	4.39E-09	1.69	This work
$\text{H}_3^+ + \text{NCN} \rightarrow \text{HNCN}^+ + \text{H}_2$	0.33	2.59E-09	1.69	This work
$\text{H}_3^+ + \text{NCN} \rightarrow \text{CN}^+ + \text{NH} + \text{H}_2$	0.33	2.59E-09	1.69	This work
$\text{H}_3^+ + \text{NCN} \rightarrow \text{CN} + \text{NH}^+ + \text{H}_2$	0.33	2.59E-09	1.69	This work
$\text{H}_3\text{O}^+ + \text{NCN} \rightarrow \text{HNCN}^+ + \text{H}_2\text{O}$	0.33	1.21E-09	1.69	This work
$\text{H}_3\text{O}^+ + \text{NCN} \rightarrow \text{CN}^+ + \text{NH} + \text{H}_2\text{O}$	0.33	1.21E-09	1.69	This work
$\text{H}_3\text{O}^+ + \text{NCN} \rightarrow \text{CN} + \text{NH}^+ + \text{H}_2\text{O}$	0.33	1.21E-09	1.69	This work
$\text{HCO}^+ + \text{HNCN} \rightarrow \text{HNCN}^+ + \text{CO}$	0.33	1.06E-09	1.69	This work
$\text{HCO}^+ + \text{HNCN} \rightarrow \text{CN}^+ + \text{NH} + \text{CO}$	0.33	1.06E-09	1.69	This work
$\text{HCO}^+ + \text{HNCN} \rightarrow \text{CN} + \text{NH}^+ + \text{CO}$	0.33	1.06E-09	1.69	This work
Neutral-neutral	$(\text{cm}^3\text{s}^{-1})$	(-)	(-)	
$\text{NH}_2 + \text{HNC} \rightarrow \text{NH}_2\text{CN} + \text{H}$	8.05E-10	0.5	2.69E+03	This work
$\text{NH}_2 + \text{CH}_2 \rightarrow \text{HNCNH} + \text{H}$	9.46E-10	0.5	5.76E+03	This work
$\text{HNCNH} + \text{H} \rightarrow \text{HNCN} + \text{H}$	1.70E-10	0.5	5.03E+03	This work
$\text{NH}_2\text{CN} + \text{H} \rightarrow \text{HNCN} + \text{H}$	7.75E-10	0.5	6.34E+03	This work
$\text{HNCNH} + \text{OH} \rightarrow \text{HNCN} + \text{H}_2\text{O}$	8.64E-10	0.5	6.62E+02	This work
$\text{NH}_2\text{CN} + \text{OH} \rightarrow \text{HNCN} + \text{H}_2\text{O}$	1.41E-11	0.0	3.28E+03	Espinosa-Garcia et al. (1993)
$\text{HNCN} + \text{OH} \rightarrow \text{HNCN} + \text{H}_2\text{O}$	8.07E-10	0.5	6.52E+02	This work
$\text{HNCN} + \text{H} \rightarrow \text{HNCN} + \text{H}_2$	1.54E-10	0.5	2.29E+03	This work
Dissociative Recombination	$(\text{cm}^3\text{s}^{-1})$	(-)	(-)	
$\text{NH}_2\text{CN}^+ + \text{e}^- \rightarrow \text{CN} + \text{NH}_2$	1.50E-07	-0.5	0	This work
$\text{NH}_2\text{CNH}^+ + \text{e}^- \rightarrow \text{HNC} + \text{NH}_2$	1.50E-07	-0.5	0	OSU database
$\text{NH}_2\text{CNH}^+ + \text{e}^- \rightarrow \text{NH}_2\text{CN} + \text{H}$	1.50E-07	-0.5	0	OSU database
$\text{NH}_2\text{CNH}^+ + \text{e}^- \rightarrow \text{HNCNH} + \text{H}$	1.50E-07	-0.5	0	This work
$\text{HNCNH}^+ + \text{e}^- \rightarrow \text{HNC} + \text{NH}$	1.50E-07	-0.5	0	This work
$\text{HNCNH}^+ + \text{e}^- \rightarrow \text{HNCN} + \text{H}$	1.50E-07	-0.5	0	This work
$\text{HNCN}^+ + \text{e}^- \rightarrow \text{H} + \text{NCN}$	1.50E-07	-0.5	0	This work
$\text{HNCNH}^+ + \text{e}^- \rightarrow \text{HNCN} + \text{H}$	1.50E-07	-0.5	0	This work
$\text{NCN}^+ + \text{e}^- \rightarrow \text{N} + \text{CN}$	1.50E-07	-0.5	0	This work

3 ASTROCHEMICAL MODEL

To investigate the formation and destruction mechanism of cyanamide and its isomer carbodiimide, we use the three-phase NAUTILUS chemical code (Rauud et al. 2016), which includes the gas, the dust grain surface and the icy mantle. The code allows us to compute abundances of chemical species with respect to time for a given set of physical and chemical parameters by setting up and solving a series of ordinary differential equations. In this study, in addition to the related reactions of cyanamide and carbodiimide, our network also includes updates of the chemistry of HNCO and its metastable isomers (Quan et al. 2010), CH₃CHNH chemistry (Quan et al. 2016), as well as the chemistry of cyanomethanimine (Zhang et al. 2020). We have added more than 200 reactions concerning NH₂CN and HNCNH. Except for gas-phase reactions as shown in Table 2, the rate constants of reactions are calculated by the corresponding equations according to Hasegawa et al. (1992), Rauud et al. (2016) on surface and mantle phases. We use the standard oxygen-rich low-metal elemental abundances. The initial abundances (Graedel et al. 1982; Quan & Herbst 2007) are listed in Table 5. All abundances are given with respect to the total hydrogen density. The code simulates chemistry in three phases and also considers various possible exchanges between the different phases via accretion, thermal and non-thermal desorption. The latter includes cosmic-ray desorption, photodesorption via external photons or those via photons produced by cosmic rays (Öberg et al. 2007), and reactive desorption using the Rice-Ramsperger-Kessel (RRK) approach (Garrod et al. 2007). The surface-mantle and mantle-surface exchange of species is also considered, such as accretion and desorption but with a smaller diffusion rate of the species compared to the processes on the surface (Rauud et al. 2016). The diffusion energy to binding energy ratio is set to be 0.5 for all species. Grains are assumed to be spherical with the radii of 0.1 μm . The density of dusts is 3 g cm⁻³ and the dust-to-gas mass ratio is 0.01.

Cyanamide has been detected in many different types of sources, while carbodiimide is only detected in Sgr B2(N) by maser emission. We classified the sources where cyanamide was detected into three categories: hot cores (e.g. Sgr B2(N), Orion KL) (Turner et al. 1975; Nummelin et al. 2000; White et al. 2003), hot corinos (e.g. IRAS 16293-2422B, NGC 1333IRA2A) (Coutens et al. 2018), and low-velocity shock regions (e.g. G+0.693, NGC 253) (Zeng et al. 2018; Martín et al. 2006). Correspondingly, to simulate how NH₂CN and HNCNH are formed and destroyed in the ISM, we applied three sets of models with different physical conditions: cold cores, hot cores/hot corinos, and shock models. Regarding G+0.693, a quiescent molecular cloud located within the Sgr B2 star-forming complex in the Central Molecular Zone (CMZ). The shock that is yielded from a cloud-cloud collision (Zeng et al. 2020), ultimately sputters icy mantles of grains efficiently. For NGC 253, the origin of the large-scale shocks is also suggested to be associated with a cloud-cloud collision (Ellingsen et al. 2017). Furthermore, NGC 253 and G+0.693 have similar physical properties, including gas kinetic temperatures and H₂ densities (Zeng et al. 2020).

In cold core models, the physical parameters remain constant with a hydrogen density of $n_{\text{H}} = n(\text{H}) + 2n(\text{H}_2) = 2 \times 10^4 \text{ cm}^{-3}$, the gas and grain temperatures of 10, 15 and 20 K, a visual extinction A_{V} of 10 mag, a cosmic ray ionization rate ζ of $1.3 \times 10^{-17} \text{ s}^{-1}$, UV factor of 1 Habing and a single grain radius of 0.1 μm .

According to the different periods of evolution, star formation can be divided into the following two stages: The first is to simulate the growth of the protostar through the accretion of the outer

envelope region, namely the freefall collapse process or prestellar phase. During this stage (1×10^6 yr), the temperature stays at a constantly low value, the density increases gradually with time, and the extinction also increases. The gas and grain temperatures were set at 10 K, the initial gas density was $3 \times 10^3 \text{ cm}^{-3}$, the final collapse density was set at two values, the low density of $1.6 \times 10^7 \text{ cm}^{-3}$, and the high density of $6 \times 10^{10} \text{ cm}^{-3}$. The second stage is the warm-up stage, during which the temperature rises according to the formula $T = T_0 + (T_{\text{max}} - T_0)(\Delta t/t_h)^n$ (Garrod & Herbst 2006), where $n = 2$, $t_h = 2 \times 10^5$ yr, $\Delta t = (t - t_0)$, $t_0 = 1 \times 10^5$ yr. After an initial cold phase of 1×10^5 yr, the gas and grain temperatures increase from 10 K to the maxima T_{max} of 150, 200 and 400 K within a time frame of 2×10^5 yr. After reaching the maximum value, the temperature remains unchanged. During this stage, the gas and dust temperatures are assumed to be well coupled. The major physical parameters of hot core/hot corino models are summarized in Table 6.

In the shock models, we use the NAUTILUS code combined with the planar magnetohydrodynamic (MHD) shock code MHD_VODE (Flower & Pineau des Forêts 2015) to simulate the chemical evolution under shock conditions. As we know, there are no signs of star formation toward G+0.693, of which the large-scale, low-velocity shocks may be yielded from a cloud-cloud collision (Zeng et al. 2020). Armijos-Abendaño et al. (2020) constrained the cloud-cloud collision age to ≤ 0.5 Myr for Sgr B2. Barnes et al. (2017) provided a broader time-scale of 0.5–0.9 Myr, assuming that clouds remain quiescent for 0.3–0.5 Myr after star formation. Therefore, before shock coming, we adopted two time-lengths of evolution stages for the cold core condition, 3×10^5 and 5×10^5 yr, respectively. The grain temperature of G+0.693 molecular cloud is ≤ 30 K (Rodríguez-Fernández et al. 2004), so we assumed that the pre-shock gas and dust temperatures were 20 and 30 K, respectively, while the pre-shock gas density is $2 \times 10^4 \text{ cm}^{-3}$. The cosmic ray ionization rate in G+0.693 is 100 or even 1000 times larger than that in the Galactic disc (Zeng et al. 2019). Accordingly, we adopted two higher cosmic ray ionization rates of 1.3×10^{-15} , and $1.3 \times 10^{-14} \text{ s}^{-1}$. In this study, we have considered weak C-type shock waves with a speed of 10 km s⁻¹. The major physical parameters of the shock wave models are summarized in Table 7.

4 RESULTS

4.1 Cold cores

Results from cold core models are shown in Fig. 2. It can be seen that cyanamide and carbodiimide are hardly produced in the gas phase, but can be slowly formed on the grain mantles at 10 K. The abundances of cyanamide and carbodiimide reach 10^{-9} and 10^{-10} on the grain at the time of $\sim 10^5$ yr, respectively. In those models, carbodiimide is mainly produced by the isomerization reaction of cyanamide on the grains. This conclusion agrees with the experiment by Duvernay et al. (2005). In the experiment, cyanamide formed carbodiimide when it was on amorphous water ice surfaces or was trapped in the water ice where the water ice acted like a catalyst and greatly lower the isomerization barrier. Therefore, cyanamide's abundance becomes lower than carbodiimide's at the time of ~ 30 yr. At 15 and 20 K, gaseous cyanamide isomers' abundance peaks are as low as $\leq 10^{-11}$, suggesting that they are still ineffectively produced. After 100 years, the cyanamide isomers are produced in a great amount on grain mantles. The maximum fractional abundances of cyanamide and carbodiimide can reach to

Table 3. Activation energy barrier values of important surface/mantle reactions.

Surface reactions	E_a (K)	Ref.
$\text{NH}_2 + \text{HNC} \rightarrow \text{NH}_2\text{CN} + \text{H}$	2.69E+03	This work
$\text{HNCN} + \text{CH}_2 \rightarrow \text{HNCNH} + \text{CH}$	5.76E+03	This work
$\text{NH}_2 + \text{CN} \rightarrow \text{NH}_2\text{CN}$	0	Coutens et al. (2018)
$\text{H} + \text{HNCN} \rightarrow \text{NH}_2\text{CN}$	0	This work
$\text{H} + \text{HNCN} \rightarrow \text{HNCNH}$	0	Yadav et al. (2019)
$\text{NH} + \text{HNC} \rightarrow \text{HNCNH}$	0	Yadav et al. (2019)
$\text{NCN} + \text{H}_2 \rightarrow \text{NH}_2\text{CN}$	0	This work
$\text{H} + \text{NCN} \rightarrow \text{HNCN}$	0	Rivilla et al. (2021)
$\text{NH} + \text{CN} \rightarrow \text{HNCN}$	0	Yadav et al. (2019)
$\text{N} + \text{CN} \rightarrow \text{NCN}$	0	This work
$\text{HNCNH} + \text{H} \rightarrow \text{HNCN} + \text{H}$	5.03E+03	This work
$\text{NH}_2\text{CN} + \text{H} \rightarrow \text{HNCN} + \text{H}$	6.34E+03	This work
$\text{HNCNH} + \text{OH} \rightarrow \text{HNCN} + \text{H}_2\text{O}$	6.64E+02	This work
$\text{NH}_2\text{CN} + \text{OH} \rightarrow \text{HNCN} + \text{H}_2\text{O}$	3.28E+03	Espinosa-Garcia et al. (1993)
$\text{HNCN} + \text{OH} \rightarrow \text{HNCN} + \text{H}_2\text{O}$	6.54E+02	This work
$\text{HNCN} + \text{H} \rightarrow \text{HNCN} + \text{H}_2$	2.29E+03	This work
$\text{NH}_2\text{CN} \rightarrow \text{HNCNH}$	4.30E+03	Duvernay et al. (2005)

Table 4. Binding energies of involved species.

Species	E_{des} (K)	Ref.
NH_2CN	5556	$\text{NH}_2 + \text{CN}$, Garrod & Herbst (2006)
HNCNH	5556	NH_2CN
HNCN	2500	$\text{NH} + \text{CN}$
NCN	2400	$\text{N} + \text{CN}$

Table 5. Initial elemental abundance of chemical models.

Species	Abundance
He	6.00×10^{-2}
N	2.14×10^{-5}
O	1.76×10^{-4}
H_2	5.00×10^{-1}
C^+	7.30×10^{-5}
S^+	8.00×10^{-8}
Si^+	8.00×10^{-9}
Fe^+	3.00×10^{-9}
Na^+	2.00×10^{-9}
Mg^+	9.00×10^{-9}
P^+	3.00×10^{-9}
Cl^+	4.00×10^{-9}
F^+	6.69×10^{-9}

10^{-7} and 10^{-8} at 15 K, and 10^{-6} and 10^{-7} at 20 K, respectively. Under these conditions, the main formation routes of cyanamide are the addition reactions of free radicals on the grain surface, $\text{NCN} + \text{H}_2$, $\text{HNCN} + \text{H}$ and $\text{NH}_2 + \text{CN}$. For carbodiimide, the major formation reaction is hydrogenation of HNCN. In these processes, even at the low temperatures, small molecules still can overcome the diffusion barriers, and react to form large molecules like NH_2CN and HNCNH on the grain surface.

4.2 Hot cores/hot corinos

Results of hot core / hot corino models are shown in Fig. 3. The leftmost panels show the variations of calculated abundances

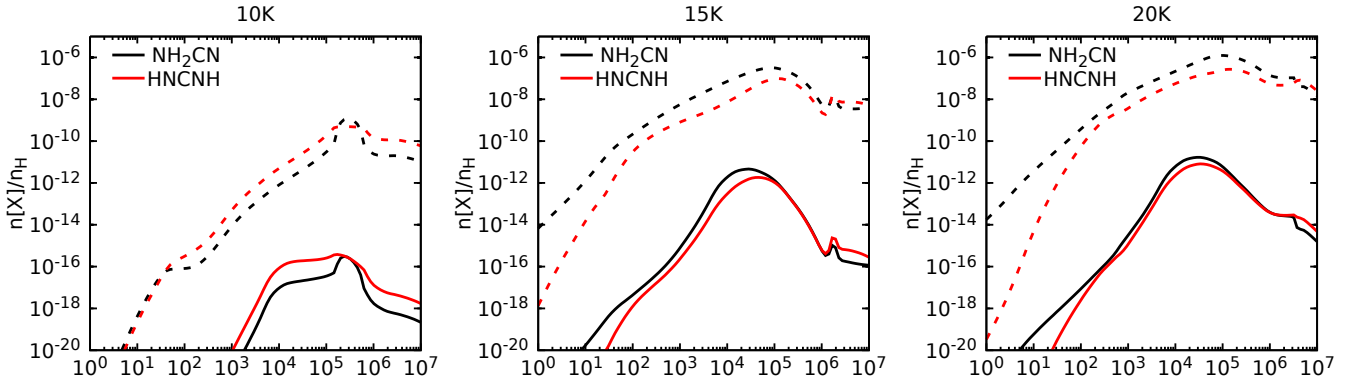
of NH_2CN and HNCNH versus time during the freefall collapse stage. In the gas phase, the two species are produced with very low abundances in two collapse densities, while they can be produced in a large amount after 4×10^5 yr on grains with the rapidly increasing density. The main formation route is the reaction of $\text{HNCN} + \text{H}$ on grain surface and icy mantle for both NH_2CN and HNCNH. Besides, NH_2CN can also be formed by the reaction of $\text{NCN} + \text{H}_2$. The maximum fractional abundance reaches 10^{-11} . We found that the two different collapse densities affect little on the fractional abundances of the isomers in gas-phase nor on grain surface.

The right two columns of Fig. 3 show computational results from four models, corresponding to different maximum temperatures in warm-up stages and different gas densities gained from the freefall collapse conditions. As shown in the two top right panels, the warm-up models can produce sufficient abundances of NH_2CN and HNCNH during the warm-up to maximum temperatures of 150 and 200 K with the hydrogen density of $1.6 \times 10^7 \text{ cm}^{-3}$. Their peak fractional abundances can reach 6×10^{-9} and 2×10^{-10} at T_{max} of 150 and 200 K, respectively. The physical parameters of top panels represent the sources of Sgr B2(N) suggested by Bonfand et al. (2019). The observational result is taken from Bellocche et al. (2013). The emission of NH_2CN corresponding to the warm component is optically thin for a source size of $2''$, the rotational temperature is 150 K, the column density is $5.13 \times 10^{16} \text{ cm}^{-2}$. In the other set of parameters, the density is 10^{13} cm^{-2} for the size of $60''$ where the gas is diluted. We adopt the hydrogen column density of $1.54 \times 10^{25} \text{ cm}^{-2}$ for the hot cores (Bonfand et al. 2017). The observed abundance of cyanamide is $\sim 3 \times 10^{-9}$. We conclude that our simulated results are in good agreement with the observation within the time range of $2.9\text{--}4.2 \times 10^5$ yr. Carbodiimide has been detected in Sgr B2(N) (McGuire et al. 2012). Its column density was anticipated to be $\sim 2 \times 10^{13} \text{ cm}^{-2}$ according to Duvernay et al. (2005), where the HNCNH abundance is $\sim 10\%$ of the abundance of NH_2CN from ice experiment. In our models, the calculated ratio of HNCNH to NH_2CN is $\sim 9.4\%$ at the time of 3.65×10^5 yr when HNCNH abundance reaches its peak for $T_{\text{max}} = 150$ K. Similarly, the ratio is $\sim 8.6\%$ at the time of 3.40×10^5 yr for $T_{\text{max}} = 200$ K. The simulated ratios are very close to the experimental value of 10%. However, when NH_2CN abundance reaches its peak value, the ratio is getting lower. In the gas phase, the isomers mainly come from the surface

Table 6. Physical parameters of hot core/hot corino models

Source(Stage)	$n_{\text{H}}(\text{cm}^{-3})$	T(K)	A_V (mag)	ζ (s^{-1})	UV factor (Habing)
The freefall collapse ^{a,b}	$3 \times 10^3 \rightarrow 1.6 \times 10^7$	10	$2 \rightarrow 6.109 \times 10^2$	1.3×10^{-17}	1
The warm-up ^{b,d}	1.6×10^7	10 \rightarrow 150, 200	6.109×10^2	1.3×10^{-17}	1, 10
The freefall collapse ^{a,c}	$3 \times 10^3 \rightarrow 6 \times 10^{10}$	10	$2 \rightarrow 1.472 \times 10^5$	1.3×10^{-17}	1
The warm-up ^{c,d}	6×10^{10}	10 \rightarrow 200, 400	1.472×10^5	1.3×10^{-17}	1

Notes. ^aGarrod & Herbst (2006), ^bBonfand et al. (2019), ^cJørgensen et al. (2016), ^dCoutens et al. (2018)

**Figure 2.** The calculated abundances of NH_2CN and HNCNH in the gas phase and on grain mantles, including surface and icy mantle, are plotted versus time for cold core models at temperatures of 10, 15, and 20 K. Solid lines correspond to the gas-phase molecules, dotted lines indicate the same species on grains.**Table 7.** Physical parameters of C-type shock models.

Parameter	Value
Initial density (cm^{-3}) n_{H}	2×10^4
Pre-shock temperature (K)	20, 30
Radiation field (Habing) UV factor	1
Cosmic ray ionization rate (s^{-1}) ζ	1.3×10^{-15} , 1.3×10^{-14}
Visual extinction (mag) A_V	10
Magnetic field strength parameter b	1.0
Shock speed (km s^{-1}) u_s	10

by thermal desorption processes. A large amount of surface NH_2CN and HNCNH desorb into the gas phase at temperature up to ~ 140 K. This agrees with the experimental results by Duvernay et al. (2005), in which the desorption temperature of HNCNH is determined to be 130–140 K. We used the same binding energy of 5556 K for both isomers, as shown in Table 4. From Fig 3, it can be seen that when the temperature increases, the two isomers' abundances rise significantly. This is because the thermal energy is sufficient to drive reactants to overcome the diffusion barriers on grain surface at ~ 50 K. During the warm-up stage, the major formation reactions are $\text{NCN} + \text{H}_2$ for NH_2CN , $\text{HNC} + \text{NH}$ for HNCNH on the grain surface. Besides, the isomers are destroyed by free radical OH on the grain surface, especially carbodiimide is. Eventually, when the temperature reaches 70 K, the isomers become to desorb efficiently, leading to their peak abundances at 140 K in the gas phase. During the warm-up stage, the two isomers desorb efficiently from the dust surface into the gas phase by thermal desorption. This agrees with the mechanism introduced by Garrod & Herbst (2006) to study interstellar complex organic molecules. After reaching the peak, the abundances of the two isomers subsequently decrease due to active destruction reactions in the gas-phase, including reactions with pos-

itive ions such as H^+ , H_3^+ , C^+ , He^+ and H_3O^+ and the free radical OH.

As shown in the two bottom right panels of Fig. 3, the warm-up models overproduce NH_2CN and HNCNH during the warm-up to T_{max} of 200 and 400 K with the hydrogen density of $6 \times 10^{10} \text{ cm}^{-3}$. The peak fractional abundances reach 3×10^{-9} for both NH_2CN and HNCNH . The physical parameters of bottom panels correspond to the source of IRAS 16293-2422B (Jørgensen et al. 2016; Coutens et al. 2018). The observational results originated from Coutens et al. (2018) and the abundance of cyanamide is derived to be $\leq 2 \times 10^{-10}$. Therefore, our simulated abundances are larger than the observation at the time range of $2.9\text{--}4.2 \times 10^5$ yr and $2.3\text{--}2.7 \times 10^5$ yr. Under the conditions of T_{max} reaches 200 and 400 K, cyanamide and carbodiimide also firstly form on the grain surface, then desorb into gas phase by thermal process when temperature increases to 70 K. The main formation reactions are the same as those described above in the case of low gas density. On the other hand, the main destruction reactions are ion-neutral reactions by H_3^+ for $T_{\text{max}} = 200$ K. Besides, there is a rapid decline of the fractional abundance of NH_2CN and HNCNH at T_{max} of 400 K. That is because at this high temperature not only the rates of formation reactions increase but destruction reactions are also faster. The latter include ion-neutral reactions by H_3^+ , and by atomic H. Although these reactions have high barriers, they can still take place at a high temperature above 200 K. The simulated ratio of NH_2CN to HNCNH is $\sim 6\%$ when HNCNH abundance reaches its peak value for T_{max} of 200 K, while the ratio is $\sim 4\%$ for T_{max} of 400 K. The cause is that the reaction barrier of $\text{HNCNH} + \text{H}$ is smaller than that of $\text{NH}_2\text{CN} + \text{H}$, as shown in Table 3. The reaction rate of the former is higher than the latter. HNCNH is more quickly destroyed than NH_2CN is.

There is high UV radiation in high mass star formation regions. Therefore, we used two higher values of UV factor, 10 and 100 times larger than the normal value for models with the hydrogen density

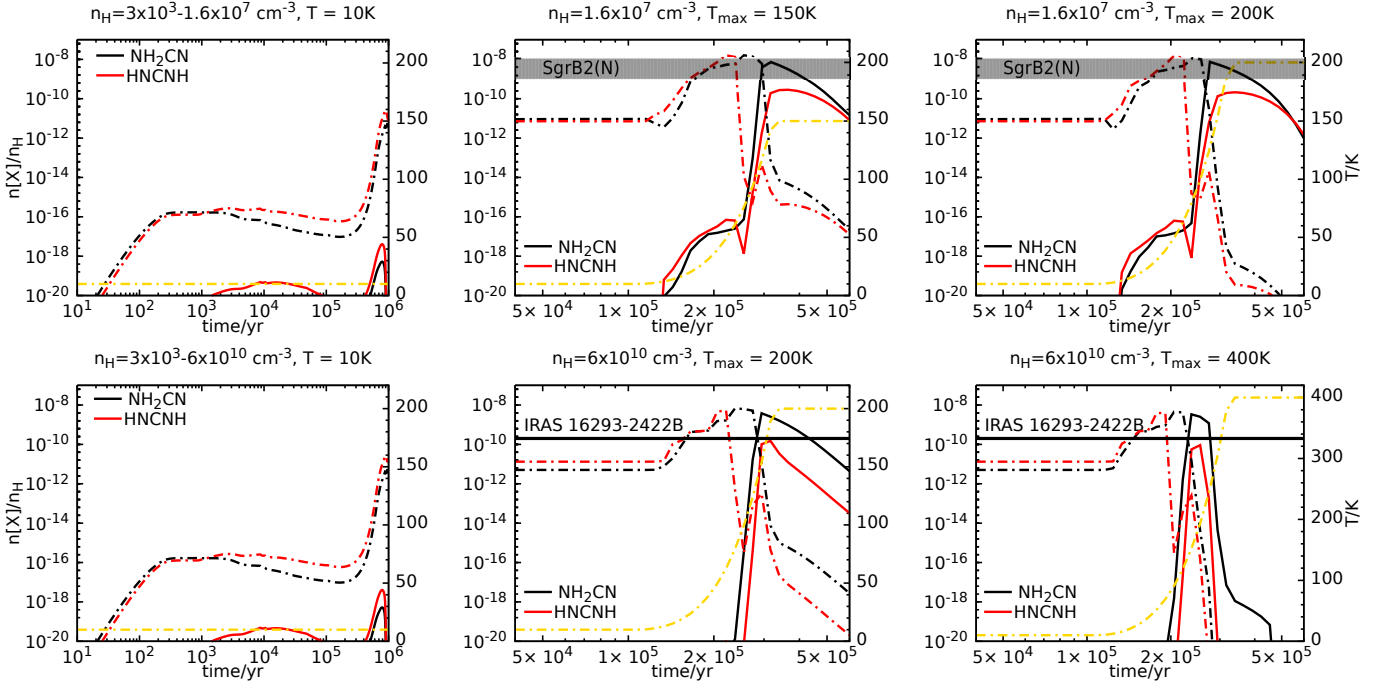


Figure 3. The calculated abundances of NH_2CN and HNCNH in the gas phase and on grain mantles, including surface and icy mantle, are plotted versus time for freefall collapse and warm-up stages in hot core/hot corino models. During the freefall collapse stage, the initial density is $3 \times 10^3 \text{ cm}^{-3}$ in both left two panels, while the final collapse densities are $6 \times 10^{10} \text{ cm}^{-3}$ and $1.6 \times 10^7 \text{ cm}^{-3}$ respectively, and the temperatures remain at a constant value of 10 K. During the warm-up stage, T_{max} adopt two values, 150 and 200 K for upper panels, and 200 and 400 K for bottom panels. Solid lines correspond to the gas-phase abundances, dotted lines indicate abundances on the grains. The gray rectangle represents the observed abundance with \pm a factor of 3 uncertainty for NH_2CN in Sgr B2(N), while the horizontal lines are showing upper limit of NH_2CN abundances toward IRAS 16293-2422B. Golden dotted lines denote temperature profiles.

of $1.6 \times 10^7 \text{ cm}^{-3}$ to further simulate the physical conditions in Sgr B2(N). In the models, only the warm-up stage adopts the high UV factor. The results are shown in Fig. 4. It can be seen that fractional abundances of cyanamide are lower comparing to the results from the standard UV factor computations for both T_{max} of 150 and 200 K. Stronger UV radiations destroy the two isomers at higher chemical reaction rates. The peak abundance of cyanamide drops from 6.79×10^{-9} to 2.98×10^{-9} at the time of $3.16 \times 10^5 \text{ yr}$ as the UV factor increases from 1 to 10 for T_{max} of 150 K. For the case of UV factor of 100, it has the same trend as the UV factor of 10, and the peak abundance of cyanamide deduced to 2.53×10^{-9} at the same time. For T_{max} of 200 K, the abundance of cyanamide reduced from 6.91×10^{-9} to 4.37×10^{-9} at the time of $2.74 \times 10^5 \text{ yr}$ when the UV factor increases from 1 to 10. With UV factor 100, the abundance of cyanamide further reduced to 3.74×10^{-9} . Fig. 4 shows that the UV factor affects more on $T_{\text{max}} = 150 \text{ K}$ than on $T_{\text{max}} = 200 \text{ K}$. The effects of UV factors 10 and 100 have a small difference on cyanamide's abundances. The simulated cyanamide abundances also agree well with the observational result within a certain time range, but it lasts a shorter period than using the standard UV factor. Although it is not shown here, the high UV factor has the same effect on the fractional abundance of carbodiimide as on that of cyanamide.

Formamide (NH_2CHO) is the simplest molecule which includes peptide bond $-\text{NH}-\text{C}(=\text{O})-$. It has been observed in a wide variety of sources including not only hot cores, hot corinos, protostellar shocked regions, but also comets. Detailed observational results are summarized in Table 1 of Lopez-Sepulcre et al. (2019). On the other hand, NH_2CN hasn't been detected in any comets so

far. It was only detected in hot and dense regions like SgrB2(N), IRAS 16293-2422B, and the source in which wide low-velocity shock waves exist, such as G+0.693. The ratio of NH_2CHO to NH_2CN varies in different types of sources (Coutens et al. 2018). In our study, NH_2CHO has the same desorption energy with NH_2CN (5556 K), which is close to the desorption energy of water, so that they have the same desorption temperature. NH_2CHO is mainly produced by the reaction of $\text{NH}_2 + \text{H}_2\text{CO} \rightarrow \text{NH}_2\text{CHO} + \text{H}$ in the gas phase (Garrod et al. 2008). We use the rate coefficient of $\text{NH}_2 + \text{H}_2\text{CO}$ in the gas phase from Skouteris et al. (2017)'s computations, and add the reaction on grain surface as well. NH_2CN is mainly produced by surface reactions of $\text{HNCN} + \text{H}$, $\text{NCN} + \text{H}_2$ and $\text{NH}_2 + \text{CN}$. NH_2CHO and NH_2CN have the competition to use NH_2 as the precursor on the grain surface. The formation reaction of formamide has a low potential barrier (4.48 K) so that it is relatively easier to form than cyanamide is. As the result, NH_2CHO exists more widely than NH_2CN in ISM. As shown in Fig. 5, in standard UV factor models, the calculated ratio of NH_2CN to NH_2CHO is 0.02 at the time of $3.16 \times 10^5 \text{ yr}$ in which both of them reach their peak abundance positions for T_{max} of 150 K. Similarly, the ratio is 0.03 at the time of $2.74 \times 10^5 \text{ yr}$ for T_{max} of 200 K. The simulated ratios agree well with the observational value of $\sim 0.02-0.04$ toward Sgr B2(N) (Coutens et al. 2018). In UV factor 10 models, the ratio of NH_2CN to NH_2CHO increases from 0.02 to 0.12 and from 0.03 to 0.36 for T_{max} of 150 K and 200 K, respectively. In UV factor = 100 models, the ratio is greater than 1. Therefore, the ratio increases with higher UV factor. A strong UV radiation inhibits the formation of NH_2CHO . Under strong UV radiation conditions, more NH_2 are destroyed by H, which are produced by photodissociation reactions.

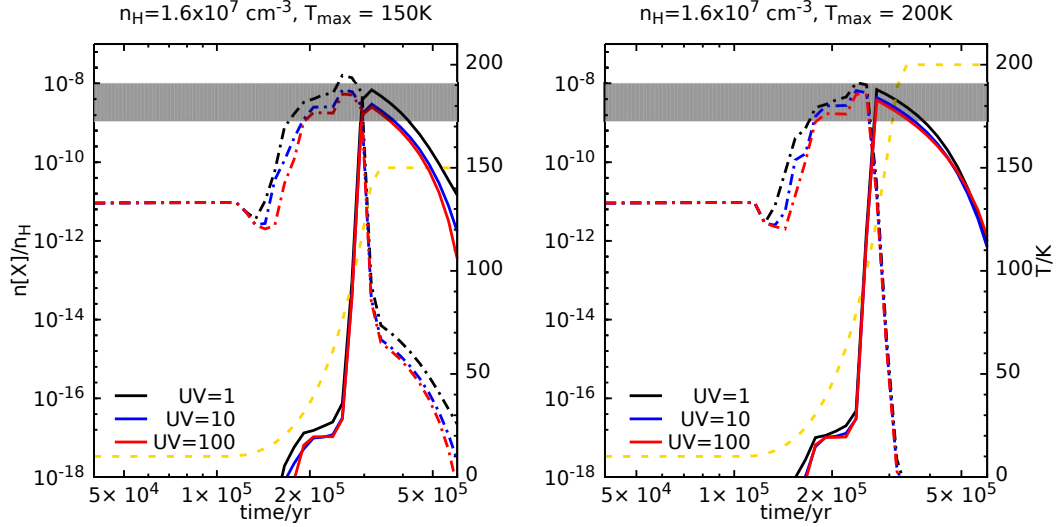


Figure 4. The calculated abundances in the gas phase and on the grain mantle, are plotted versus time for warm-up models with the gas density of $1.6 \times 10^7 \text{ cm}^{-3}$. The left panel denotes T_{max} of 150 K with different UV factors, and the right panel responds T_{max} of 200 K. Only cyanamide is shown as an example here, and carbodiimide has similar tendency. Solid lines correspond to the gas-phase abundances, dotted lines indicate abundances on the grains. The gray rectangle represents the observed abundance with \pm a factor of 3 uncertainty for NH_2CN in Sgr B2(N). Golden dotted lines denote temperature profiles.

Formation efficiency of NH_2CHO thus decreases. While it affects less on NH_2CN , the latter has more formation routes other than from the reactant NH_2 .

4.3 C-type shocked regions

Results of C-type shock models are shown in Fig. 6. In the pre-shock stage, cyanamide and its isomer, carbodiimide, have been produced in a large amount on the grain surface, while the gas phase formation reactions are inefficient because of the low temperature. After shock comes at the velocity of $\sim 10 \text{ km s}^{-1}$, the gas density is increased by an order of magnitude, eventually leading to the final density of 10^5 cm^{-3} . The gas and dust temperatures rapidly increase to over five hundred Kelvin. In Fig. 6, $t = 0$ denotes the onset of the shock. At this time, cyanamide and carbodiimide abundances are taken from the exit values of the previous stage of the cold core models. Then the gaseous cyanamide and carbodiimide fractional abundances dramatically increase with the time when shock propagates. Meanwhile, grain surface abundances of these molecules decrease rapidly. The shock heats the grain and sputters molecules from the grain mantles. Comparing to the observation, all of these abundances can reach the range of the observation, but within different time periods. For $\zeta = 1.3 \times 10^{-15} \text{ s}^{-1}$, the range of time is $3.9\text{--}7.6 \times 10^2 \text{ yr}$ after $3 \times 10^5 \text{ yr}$ of cold core conditions. This range is shorter ($3.9\text{--}6.8 \times 10^2 \text{ yr}$) if the cold core evolves for $5 \times 10^5 \text{ yr}$, as shown in the top panels of Fig. 6. For $\zeta = 1.3 \times 10^{-14} \text{ s}^{-1}$, there are only a small time-window in which the result agrees with the observation, which are 50 and 40 yr with the evolution of time $t = 3 \times 10^5$ and $5 \times 10^5 \text{ yr}$ for cold core conditions, respectively, as shown in the bottom panels of Fig. 6. We found that molecular peak values can be reached at a shorter time with higher cosmic ray ionization rates. That is because stronger cosmic ray accelerates the formation reactions of free radical so that larger molecules form more quickly on grain surface. Using high cosmic ray ionization rates reduces the time to reach peak abundances. Besides, the two isomers' abundances reach the range of observation on the grain surface before the shock comes under cold core conditions with the evolution of

time $t = 3 \times 10^5$ and $5 \times 10^5 \text{ yr}$. As the result, their gas phase abundances may agree with the observation after shock sputters them off the dust grains. The final temperature varies with the value of ζ . In addition, when ζ is $1.3 \times 10^{-15} \text{ s}^{-1}$, the post-shock temperature stays at $\leq 65 \text{ K}$. Therefore, small species accrete back on the grain from the gas phase, and complex organic molecules (COMs) will form on grain surface, like cyanamide and carbodiimide, as shown in top panels of Fig. 6. When ζ is $1.3 \times 10^{-14} \text{ s}^{-1}$, all species have been sputtered by shock into gas phase at peak temperatures (above 1000 K). Then the temperature starts to drop, still above 130 K. Almost all cyanamide molecules no longer exist on grain as the temperature is equal to its' desorption temperature. Molecules that are smaller than cyanamide are hard to deplete on grain. So, there are no COMs like cyanamide could form on grain surfaces. Two examples are shown in bottom panels of Fig. 6. For pre-shock temperature of 30K, our results agree with the observation using $\zeta = 1.3 \times 10^{-14} \text{ s}^{-1}$, but this is not for the case for $\zeta = 1.3 \times 10^{-15} \text{ s}^{-1}$. In the shock models, the origin of cyanamide and carbodiimide is also from the grain surface by free radical reactions, which are $\text{NH}_2 + \text{CN}$, $\text{HNCN} + \text{H}$ and $\text{NCN} + \text{H}_2$ for cyanamide, and $\text{HNCN} + \text{H}$ for carbodiimide. This is similar to results under cold core conditions. So, we speculated that the two isomers are mainly formed by sublimation process to release COMs, which were previously formed in the solid phase, into the gas phase. The destruction reactions include cosmic ray induced photodissociation, and ion-neutral reactions by H_3^+ , H_3O^+ for ζ of $1.3 \times 10^{-15} \text{ s}^{-1}$. When ζ is $1.3 \times 10^{-14} \text{ s}^{-1}$, the destruction reactions are ion-neutral reactions by H^+ and the reaction of $\text{NH}_2\text{CN}/\text{HNCNH} + \text{H}$. According to our calculations, a strong cosmic ray ionization ($\zeta \geq 10^{-15} \text{ s}^{-1}$), shortens the time for the isomers to reach their peak abundances, and decreases the efficiency of their formation on dust grains.

As a precursor of cyanamide and carbodiimide, HNCN also has been detected toward G+0.693 with the abundance of 9.1×10^{-11} , which is an order of magnitude lower than cyanamide abundance. Our simulated results reach $\sim 10^{-9}$, one order of magnitude larger than the observational result, but the high abundance of HNCN only

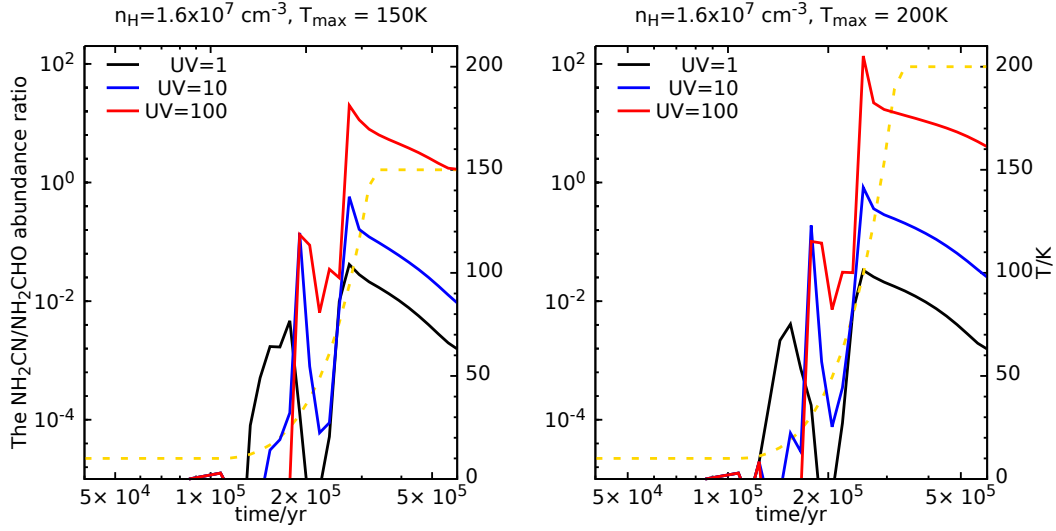


Figure 5. The calculated abundance ratios between the NH_2CN and NH_2CHO in the gas phase are plotted versus time for warm-up models with the gas density of $1.6 \times 10^7 \text{ cm}^{-3}$. The left panel denotes T_{max} of 150 K with different UV factors, and the right panel responds T_{max} of 200 K. Golden dotted lines denote temperature profiles.

lasts a very short period of time because HNCN is rapidly converted into cyanamide and carbodiimide by hydrogenation.

According to Merz et al. (2014), NH_2CN , HNCNH and C_3NH may create a tautomer of adenine with retrosynthetic analysis. The three molecules are all detected in ISM, but are in different types of sources. So far, C_3NH was only detected in a standard cold core TMC-1, cyanamide was mainly detected in hot cores/corinos or shock regions, and carbodiimide was only detected in the hot core Sgr B2(N). Therefore, we preliminarily infer that they are produced under different physical conditions, and it is very unlikely that they could appear in the same region. C_3NH 's fractional abundance is $\sim 2 \times 10^{-11}$ from our shock models. This agrees with the suggested value of 1.5×10^{-11} in the tentative detection by Zeng et al. (2018). Besides, the three-body reaction to form the tautomer is hard to occur in ISM.

5 CONCLUSIONS

In this work, we ran chemical simulations to calculate the evolution of NH_2CN and HNCNH in ISM. The main results are summarized as follows:

1. Cyanamide has been formed during the prestellar phase in hot cores or hot corinos. The formation process is interpreted as resulting from the sublimation of the icy mantles of dust grains. This agrees with the observations that this molecule generally has been found in the compact and hot regions with $T \geq 100 \text{ K}$. A similar process could also occur through shocks, like in the region of G+0.693 where cyanamide was detected.

2. Our modelling results suggest that cyanamide and carbodiimide molecules come from surface chemistry formation at early evolutionary stages. They are subsequently released back to the gas phase, either by thermal process (in hot cores or hot corinos) or by shock-induced desorption (in shock regions). Comparing with the observations, our simulations are well verified. We found that cyanamide and carbodiimide are mainly formed by free radical reactions on dust grain surfaces, and are destroyed by positive ions in gas phase, as well as OH and H both in gas phase and on grain sur-

faces. The two isomers are difficult to form in gas phase because of high barriers of gaseous formation reactions. Thus, they are unlikely to be detected in the cold dark cloud cores.

3. Strong UV radiation significantly lower the abundances of cyanamide and carbodiimide. Stronger UV destroys the two isomers with faster chemical reaction rates. Besides, from high UV factor models, the ratio of NH_2CN to NH_2CHO increases comparing to a standard UV factor.

4. Strong cosmic ray ionization shortens the time for the isomers to reach peak abundances, and decreases the efficiency of their formation on dust grains.

5. C_3NH is formed by gas reactions at low temperatures, and its fractional abundance is low in our simulations where cyanamide has relatively high abundances. Therefore, it is an inefficient route to form a tautomer of adenine by starting from molecules C_3NH , HNCNH and NH_2CN in ISM.

ACKNOWLEDGEMENTS

This work was supported by the Natural Science Foundation of Xinjiang Uygur Autonomous Region (2022D01A156), the National Key R&D Program of China (No.2022YFA1603103), the "Tianchi Doctoral Program 2021", the National Natural Science Foundation of China under grant 12203091, 11973075, 12173075.

DATA AVAILABILITY STATEMENT

The datasets generated during this study are available in the article and from the corresponding author upon request.

REFERENCES

- Aladro R., Martín S., Martín-Pintado J., Mauersberger R., Henkel C., Ocaña Flaquer B., Amo-Baladrón M. A., 2011, *A&A*, **535**, A84
 Armijos-Abendaño J., Banda-Barragán W. E., Martín-Pintado J., Dénes H., Federrath C., Requena-Torres M. A., 2020, *MNRAS*, **499**, 4918

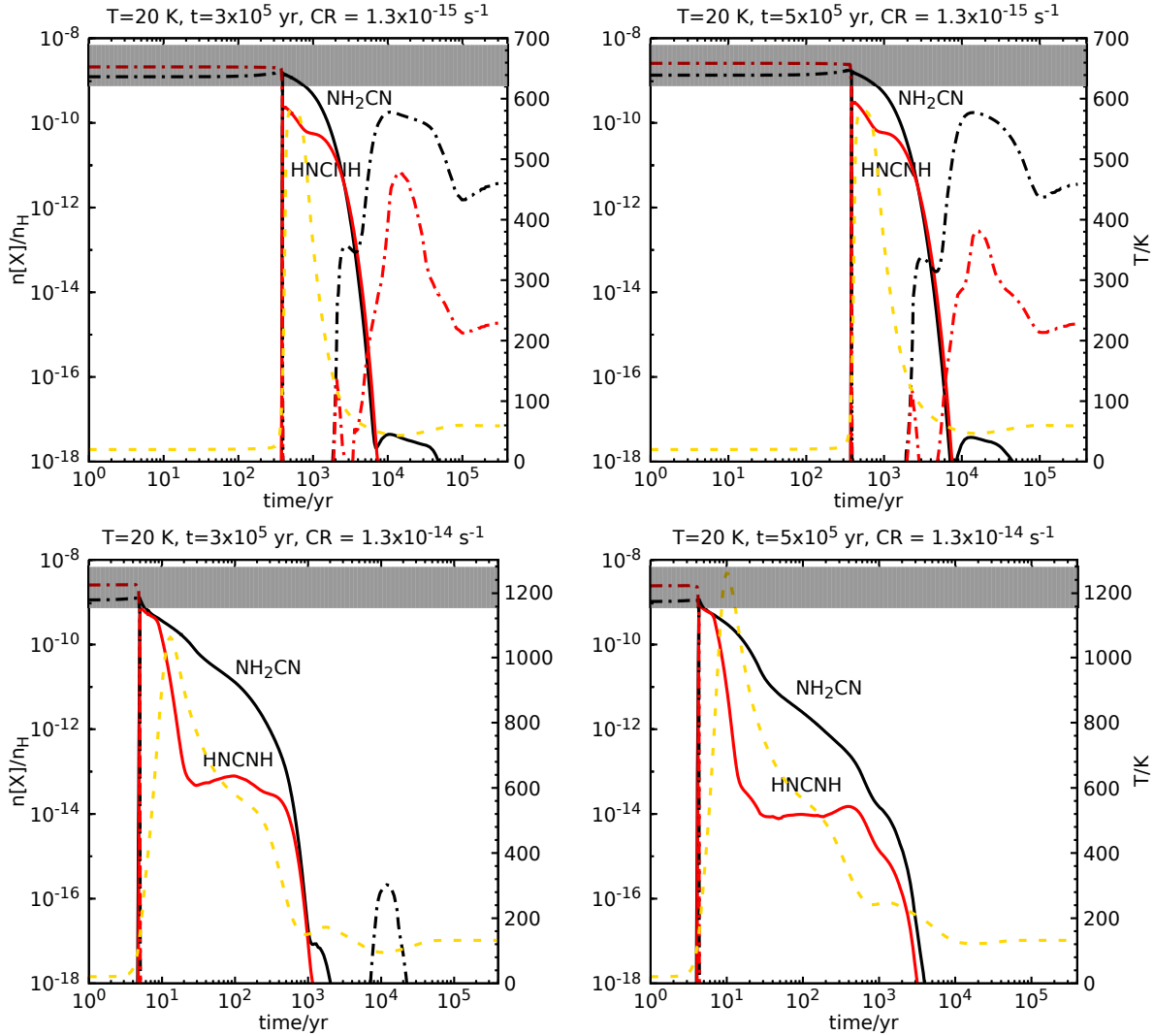


Figure 6. The calculated abundances of NH_2CN and HNCNH in the gas phase and on grain mantles, including surface and icy mantle for our C-type shock models. The results are plotted versus time after cold core models with the evolution time of 3, 5×10^5 yr at pre-shock temperatures of 20 K with higher ζ . Solid lines correspond to the gas-phase abundances, and dotted lines indicate abundances on the grains. The gray rectangle represents the observed abundance with \pm a factor of 3 uncertainty for NH_2CN in G+0.693. Golden dotted lines denote temperature profiles.

Barnes A. T., Longmore S. N., Battersby C., Bally J., Kruijssen J. M. D., Henshaw J. D., Walker D. L., 2017, *MNRAS*, **469**, 2263
 Belloche A., Müller H. S. P., Menten K. M., Schilke P., Comito C., 2013, *A&A*, **559**, A47
 Belloche A., Garrod R. T., Müller H. S. P., Menten K. M., Medvedev I., Thomas J., Kisiel Z., 2019, *A&A*, **628**, A10
 Belloche A., et al., 2020, *A&A*, **635**, A198
 Bise R. T., Choi H., Neumark D. M., 1999, *The Journal of chemical physics*, **111**, 4923
 Bise R. T., Hoops A. A., Neumark D. M., 2001, *The Journal of Chemical Physics*, **114**, 9000
 Blitz M. A., Seakins P. W., Smith I. W. M., 2009, *Physical Chemistry Chemical Physics (Incorporating Faraday Transactions)*, **11**, 10824
 Bonfand M., Belloche A., Menten K. M., Garrod R. T., Müller H. S. P., 2017, *A&A*, **604**, A60
 Bonfand M., Belloche A., Garrod R. T., Menten K. M., Willis E., Stéphan G., Müller H. S. P., 2019, *A&A*, **628**, A27
 Brack A., 1999, *Advances in Space Research*, **24**, 417
 Chakrabarti S., Chakrabarti S. K., 2000, *A&A*, **354**, L6
 Chakrabarti S. K., Majumdar L., Das A., Chakrabarti S., 2015, *Ap&SS*,

357, 90
 Coutens A., et al., 2018, *A&A*, **612**, A107
 Cummins S. E., Linke R. A., Thaddeus P., 1986, *ApJS*, **60**, 819
 De Becker M., 2013, *Bulletin de la Societe Royale des Sciences de Liege*, **82**, 33
 Dunning Thom H. J., 1989, *J. Chem. Phys.*, **90**, 1007
 Duvernoy F., Chiavassa T., Borget F., Aycard J.-P., 2004, *Journal of the American Chemical Society*, **126**, 7772
 Duvernoy F., Chiavassa T., Borget F., Aycard J.-P., 2005, *The Journal of Physical Chemistry A*, **109**, 603
 Ellingsen S. P., Chen X., Breen S. L., Qiao H. H., 2017, *MNRAS*, **472**, 604
 Enrique-Romero J., Rimola A., Ceccarelli C., Ugliengo P., Balucani N., Skouteris D., 2019, *ACS Earth and Space Chemistry*, **3**, 2158
 Espinosa-Garcia J., Corchado J., Sana M., 1993, *Journal de Chimie Physique*, **90**, 1181
 Flower D. R., Pineau des Forêts G., 2015, *A&A*, **578**, A63
 Frisch M. J., et al., 2016, *Gaussian 16*, Revision A.03. Gaussian, Inc., Wallingford, CT, USA
 Fukui K., 1981, *Accounts of chemical research*, **14**, 363
 Garrod R. T., Herbst E., 2006, *A&A*, **457**, 927

- Garrod R. T., Wakelam V., Herbst E., 2007, *A&A*, **467**, 1103
- Garrod R. T., Widicus Weaver S. L., Herbst E., 2008, *ApJ*, **682**, 283
- Goerigk L., Grimme S., 2011, *Journal of chemical theory and computation*, **7**, 291
- Graedel T. E., Langer W. D., Frerking M. A., 1982, *ApJS*, **48**, 321
- Grimme S., 2006, *J. Chem. Phys.*, **124**, 034108
- Grimme S., Ehrlich S., Goerigk L., 2011, *Journal of computational chemistry*, **32**, 1456
- Harada N., Herbst E., Wakelam V., 2010, *ApJ*, **721**, 1570
- Hasegawa T. I., Herbst E., Leung C. M., 1992, *ApJS*, **82**, 167
- He Y., Liu X., Lin M. C., Melius C. F., 1991, *International Journal of Chemical Kinetics*, **23**, 1129
- Jabs W., Winnewisser M., Belov S. P., Lewen F., Maiwald F., Winnewisser G., 1999, *Molecular Physics*, **97**, 213
- Jørgensen J. K., et al., 2016, *A&A*, **595**, A117
- Kawaguchi K., et al., 1992, *ApJ*, **396**, L49
- Kilpatrick M. L., 1947, *Journal of the American Chemical Society*, **69**, 40
- Ligterink N. F. W., El-Abd S. J., Brogan C. L., Hunter T. R., Remijan A. J., Garrod R. T., McGuire B. M., 2020, *ApJ*, **901**, 37
- Lopez-Sepulcre A., Balucani N., Ceccarelli C., Codella C., Dulieu F., Theule P., 2019, *ACS Earth and Space Chemistry*, **3**, 2122
- Marcelino N., et al., 2018, *A&A*, **620**, A80
- Martín S., Mauersberger R., Martín-Pintado J., Henkel C., García-Burillo S., 2006, *ApJS*, **164**, 450
- McGuire B. A., et al., 2012, *ApJ*, **758**, L33
- Merz Kenneth M. J., Aguiar E. C., da Silva J. B. P., 2014, *Journal of Physical Chemistry A*, **118**, 3637
- Nummelin A., Bergman P., Hjalmarsen Å., Friberg P., Irvine W. M., Millar T. J., Ohishi M., Saito S., 2000, *ApJS*, **128**, 213
- Öberg K. I., Fuchs G. W., Awad Z., Fraser H. J., Schlemmer S., van Dishoeck E. F., Linnartz H., 2007, *ApJ*, **662**, L23
- Palau A., et al., 2017, *MNRAS*, **467**, 2723
- Papajak E., Leverentz H. R., Zheng J., Truhlar D. G., 2009, *Journal of chemical theory and computation*, **5**, 1197
- Purvis III G. D., Bartlett R. J., 1982, *The Journal of Chemical Physics*, **76**, 1910
- Puzzarini C., Salta Z., Tasinato N., Lupi J., Cavallotti C., Barone V., 2020, *MNRAS*, **496**, 4298
- Quan D., Herbst E., 2007, *A&A*, **474**, 521
- Quan D., Herbst E., Osamura Y., Roueff E., 2010, *ApJ*, **725**, 2101
- Quan D., Herbst E., Corby J. F., Durr A., Hassel G., 2016, *ApJ*, **824**, 129
- Rathborne J. M., et al., 2015, *ApJ*, **802**, 125
- Rivilla V. M., et al., 2021, *MNRAS*, **506**, L79
- Rodríguez-Fernández N. J., Martín-Pintado J., Fuente A., Wilson T. L., 2004, *A&A*, **427**, 217
- Ruaud M., Wakelam V., Hersant F., 2016, *MNRAS*, **459**, 3756
- Scuseria G. E., Schaefer III H. F., 1989, *The Journal of Chemical Physics*, **90**, 3700
- Scuseria G. E., Janssen C. L., Schaefer III H. F., 1988, *The Journal of Chemical Physics*, **89**, 7382
- Skouteris D., Vazart F., Ceccarelli C., Balucani N., Puzzarini C., Barone V., 2017, *MNRAS*, **468**, L1
- Sleiman C., El Dib G., Talbi D., Canosa A., 2018a, *ACS Earth and Space Chemistry*, **2**, 1047
- Sleiman C., El Dib G., Rosi M., Skouteris D., Balucani N., Canosa A., 2018b, *Physical Chemistry Chemical Physics*, **20**, 5478
- Smith I. W. M., Talbi D., Herbst E., 2001, *A&A*, **369**, 611
- Smith I. W. M., Herbst E., Chang Q., 2004, *MNRAS*, **350**, 323
- Steinman G., Lemmon R. M., Calvin M., 1964, *Proceedings of the National Academy of Sciences of the United States of America*, **52**, 27
- Talbi D., Smith I. W. M., 2009, *Physical Chemistry Chemical Physics (Incorporating Faraday Transactions)*, **11**, 8477
- Tordini F., Bencini A., Bruschi M., De Gioia L., Zampella G., Fantucci P., 2003, *The Journal of Physical Chemistry A*, **107**, 1188
- Turner B. E., Liszt H. S., Kaifu N., Kisliakov A. G., 1975, *ApJ*, **201**, L149
- White G. J., Araki M., Greaves J. S., Ohishi M., Higginbottom N. S., 2003, *A&A*, **407**, 589
- Williams A., Ibrahim I. T., 1981, *Chemical Reviews*, **81**, 589
- Woon D. E., Herbst E., 2009, *Astrophysical Journal Supplement Series*, **185**, 273
- Yadav M., Misra A., Tandon P., et al., 2019, *Origins of Life and Evolution of Biospheres*, **49**, 89
- Zeng S., et al., 2018, *MNRAS*, **478**, 2962
- Zeng S., Quénard D., Jiménez-Serra I., Martín-Pintado J., Rivilla V. M., Testi L., Martín-Doménech R., 2019, *MNRAS*, **484**, L43
- Zeng S., et al., 2020, *MNRAS*, **497**, 4896
- Zhang X., Quan D., Chang Q., Herbst E., Esimbek J., Webb M., 2020, *MNRAS*, **497**, 609

This paper has been typeset from a $\text{\TeX}/\text{\LaTeX}$ file prepared by the author.